Hydrodynamic optimization of the impeller and diffuser vane of an axial-flow pump

Duc-Anh Nguyen[1,2], Sang-Bum Ma[2], Sung Kim[2] and Jin-Hyuk Kim[1,2]

[1]Convergence Manufacturing System Engineering (Green Process and Energy System Engineering), University of Science and Technology, 217, Gajeong-ro, Yuseong-gu, Deajeon 34113, Korea, [2]Carbon Neutral Technology R&D Department, Korea Institute of Industrial Technology, 89 Yangdaegiro-gil, Ip-jang-myeon, Seobuk-gu, Cheonan-si, Chungcheongnam-do 31056, Korea

Abstract   Enhancing the hydraulic performance of an axial-flow pump is necessary for increasing the working efficiency and reducing the costs of the pump. In the present study, the impeller and diffuser vane geometry of an axial flow pump are optimized to improve the total efficiency and total head. The internal flow field was obtained by solving the steady-state Reynolds-averaged Navier-Stokes equations in the k-ω shear stress transport reattachment modification turbulence model. The structure was modeled on a hexahedral mesh with a small y+ value at all walls. The total efficiency and total head were chosen as the objective functions in two multi-objective optimizations: one for the impeller with four design variables (shroud chord length, hub chord length, inlet blade angle at mid span, and stagger angle at mid span), the other for the diffuser vane with four design variables (hub radius at the trailing edge, hub position at the leading edge, hub blade angle at the leading edge and middle blade angle at the leading edge). These design variables were selected because they sensitively affect the objective functions, as confirmed using the screening technique based on the 2k factorial method. The blades were optimized by an approximation function based on the following surrogate models: response surface approximation, kriging meta, and a radial basis neural network. After optimizing the impeller, the total efficiency and total head were 0.974 % and 21.028 % higher respectively, than those of the reference impeller, and after optimizing the diffuser vane, the total efficiency and total head were 3.097 % and 10.205 % higher, respectively, than those of the reference model.

1. Introduction

Axial-flow pumps have a simple structure and compact size, yet are sturdy and deliver high performance and a large flow rate. Owing to these advantages, axial-flow pumps are commonly selected for pumping stations and water supply facilities. The research, design and manufacture of axial flow pumps are expected to improve the quality of pump products for agriculture and industrial sectors, boosting the economic efficiency of these sectors.

Typical axial flow pumps contain an inlet guide vane, an impeller, and a diffuser vane. Each of these main parts influences the operation of the pump. Many studies have reported that the tip clearance of the impeller directly affects the stable operation of the pump [1-5]. Clearly, the design and optimization process is crucial for achieving axial flow pumps with high hydraulic performance. To concurrently increase the efficiency and the pressure head, Kim et al. [6] optimized the sweep angle and pitch angle of the impeller through a multi-objective evolutionary algorithm combined with a response surface approximation (RSA) model. After optimization, the total efficiency and pressure head were 7.51 % and 0.19 % higher than in the original design, respectively. The performance enhancement was mainly attributed to vortex elimination in the diffuser vane zone. To further improve the hydraulic performance, Kim et al. [6] optimized the diffuser vane with two design variables, namely, the inlet angle and the diffuser vane length.

The finally optimized design improved the total efficiency and pressure head by 9.03 % and 4.61 % from those of the reference case, respectively. Suh et al. [7] optimized the hub and shroud inlet angle in the second stage of a multi-phase pump. Their multi-objective optimization simultaneously improved the efficiency and total pressure of the impeller model by 1.1 % and 16.3 kPa, respectively. Meanwhile, in the optimum diffuser-vane model, the static efficiency and static pressure were enhanced by 3.1 % and 27 kPa, respectively. The hydraulic performance was mainly improved by the reduced discordance between the blade and flow angles from inlet to outlet. Shi et al. [8] used a multi-disciplinary optimization design method to enhance the impeller mass and performance of the axial flow pump. In the optimal model, the mass of a single impeller was decreased by 10.47 % and the total efficiency increased from 93.91 % to 94.49 %. In addition, the shortened blade length improved the structural strength of the optimal model from that of the base model.

Besides optimizing the blade shape, Mu et al. [9] improved the hydrodynamic performance of an axial flow pump by creating grooves in the pump wall. The flow control technology by the groove shape significantly improved the hydrodynamic performance of the pump. Especially under the deep stall condition, the pressure head of the pump was enhanced by 85.55 %. The grooves effectively improved the inflow and reduced the flow separation on the impeller surface. Zhang et al. [10] improved the hydraulic performance of a helico-axial multiphase pump with multi-objective optimization. The efficiency and pressure head were 3 % and 10 % higher in the optimal model than in the reference model, respectively. Zhang et al. [11] performed a multi-objective optimization with main design variables that decreased the pressure pulsation in an axial flow pump. The pressure head was increased by 4.26 % and 17.8 % from that of the reference model, respectively, and the pressure pulsation and shaft power were 11 % and 1.22 % lower than in the reference model, respectively. The optimized model improved the smoothness and uniformity of the flow and suppressed the high pressure at the hub of the impeller.

Meng et al. [12] also carried out a multi-objective optimization of the impeller and diffuser vane based on an artificial neural network (ANN). Under the reverse-design condition, the efficiency and pressure head were 18.62 % and 60.4 % higher in the optimized design than in the reference design, respectively. Miao et al. [13] modified the particle swarm optimization (PSO) algorithm for multiple optimization of the impeller in an axial flow pump. The modified PSO algorithm required less computational time and found the solution in fewer iterations. The study confirmed the feasibility of swarm intelligence in optimizing the impeller shape of the axial flow pump. Jung et al. [14] optimized the shape of the impeller in an axial flow pump using a polynomial surrogate model. The new design improved the flow stability and increased the pressure head and total efficiency by 17 % and 5.6 %, respectively, from those of the initial design.

Multi-objective optimization of the centrifugal pump has also been widely reported. Wang et al. [15] performed a multi-objective optimization of the cavitation performance in a centrifugal pump. They coupled an ANN with the non-dominated sorting genetic algorithm II. The cavitation performance at off-design was significantly higher in the optimum model than in the original model. Moreover, the suction efficiency at the design point was 6.9 % higher than in the reference model. To improve the hydraulic performance and reduce the vibration intensity of a marine centrifugal pump, Wang et al. [16] optimized the impeller of the pump using Latin hypercube. The optimization improved the pressure pulsation and increased the efficiency by 4.3 % from that of the base model while decreasing the vibration intensity by 30.5 %. Shim and Kim [17] performed a multi-objective optimization based on the RSA method to increase the hydraulic performance of a centrifugal pump. After optimization, the flow instability was eliminated and the pump operated with high efficiency and stability. To enlarge the operating range of an efficiently operating pump, Wang et al. [18] performed a multi-objective optimization based on ANN, Kriging (KRG), and a hybrid approximation model. The optimization improved the efficiency by 1.63 %, 1.95 %, and 4.94 % at 0.8 Q_d, 1.0 Q_d, and 1.2 Q_d, respectively, from those of the reference model (here, Q_d is the flow rate) and simultaneously improved the turbulence kinetic energy and secondary flow. Wang et al. [19] also applied ANN-based multi-objective optimization to a double-suction centrifugal pump. The results showed a notably enhanced suction efficiency at both the design and off-design points. Multi-objective optimization has increased the hydraulic performance of many other types of devices [20-25]. These studies also demonstrated higher efficiency and pressure head of the optimized models than of the reference designs.

In most of the current studies, the hydraulic performance of the pump was improved by changing the blade shape. As demonstrated in the above studies, algorithms that can find the optimal design have clearly improved the hydraulic performance of pumps. Therefore, in this work, the impeller and the diffuser vane of the axial flow pump are optimized by constructing an approximation function based on three surrogate models: RSA, KRG, and a radial basis neural network (RBNN). For maximizing the hydraulic performance of the axial flow pump, the total efficiency and total head of the pump are simultaneously increased through multi-objective optimization. The performances of the initial and optimized models are compared by analyzing their internal flow fields.

2. Specification and axial flow pump model

Fig. 1 depicts the axial flow pump model in this study. The model contains three main parts: an inlet guide vane with four blades, a rotating impeller with four blades, and a stationary diffuser with seven blades. The hydraulic design ignores the impeller tip clearance which exists in the actual pump model. The impeller diameter ratio, defined as the ratio of the hub diameter to the impeller shroud, was 0.2703. The model was

scaled to 1/8 of the real model. The inlet and outlet sections of the axial pump were extended to approximately four times the diameter of the impeller blade to prevent their interference with the flow field in the pump. The design flowrate coefficient and head coefficient were 0.4319 and 1.5841, respectively. Other design parameters are given in Table 1. Ideally, the four inlet guide vane (IGV) blades, four impeller blades, and seven diffuser vane blades should be modelled in the computational domain to simulate the true flow field. However, exploiting the geometric symmetry of the axial pump, the computational model was constructed with one IGV blade, one impeller blade, and two diffuser vane blades with a pitch ratio of 1.00:1.00:1.14. This pitch ratio should approximate 1.0 to maximize the accuracy and to minimize the profile scaling [26]. For this reason, two diffuser vane blades were placed in the computational domain.

The impeller was optimized in the first optimization process. The effect of the changes and best parameters of the impeller blade were determined with one impeller part in the computational model. In the second optimization, the diffuser vane was optimized in the computational model with all three parts: the IGV, impeller, and diffuser vane. The specific speed, flow rate coefficient, head coefficient and rotational speed coefficient were respectively calculated as follows:

$$n_q = n\left[rpm\right]\frac{Q^{0.5}\left[\dfrac{m^3}{min}\right]}{H^{0.75}\left[m\right]} \qquad (1)$$

$$\varphi = \frac{Q}{nD^3} \qquad (2)$$

$$\psi = \frac{gH}{n^2 D^2} \qquad (3)$$

$$\phi = \frac{nD}{\sqrt{gH}} \qquad (4)$$

where Q, n, D, g and H denote the flow rate, rotational speed, impeller diameter, gravitational acceleration, and pressure head, respectively.

3. Numerical analysis method

The internal flow fluid field and hydraulic characteristics of the axial flow pump were analyzed using the ANSYS CFX-19.0 commercial code software [26]. The grid system is shown in Fig. 2. Grid independence was checked using the grid convergence index (GCI) [27] and the optimum grid was identified as described in a previous study [28]. The grid dependence was sequentially checked on the impeller, IGV, and diffuser vane with a grid refinement factor of 1.3. The head coefficient was selected as the key variable. The fine-grid convergence index (GCI_{fine}^{21}) values of the impeller, IGV, and diffuser vane were 0.037, 0.0036 and 0.0025, respectively, with extrapolated relative errors (e_{ext}^{21}) of 0.0065, 0.2861 and 0.2033, respectively, as shown in Table 2. The low GCI_{fine}^{21} and e_{ext}^{21} values indicate that the created grids were optimal and required no further mesh refinement. A structured grid system for one blade was created using ANSYS TurboGrid [26] with 530000 nodes for the inlet guide vane, 560000 nodes for the impeller, and

Table 1. Design specification of the axial flow pump.

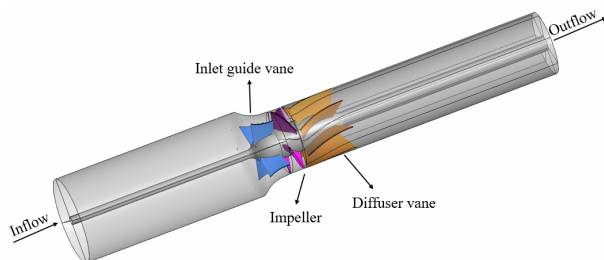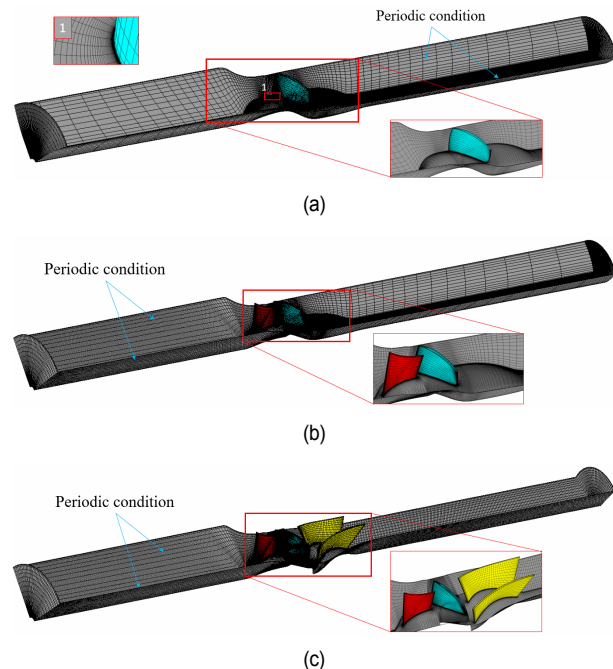| Parameter	Value
Specific speed	1204
Impeller diameter ratio	0.2703
Design rotational speed coefficient	0.7893
Design head coefficient	1.5841
Design flowrate coefficient	0.4319
Number of inlet guide vanes (EA)	4
Number of impeller blades (EA)	4
Number of diffuser vanes (EA)	7

Fig. 1. Axial flow pump model.

Fig. 2. Grid system of the axial flow pump: (a) only impeller (used in impeller optimization); (b) IGV and impeller, (c) full components (used in DV optimization).

Table 2. Results of the grid convergence index analysis.

	Impeller only (No. of grid of impeller part)	IGV and impeller (No. of grid of IGV part)	Full components (No. of grid of DV part)
N_1	557752	530472	587884
N_2	288920	242947	250480
N_3	111135	131595	140740
r	1.3	1.3	1.3
ψ_1 / ψ_1	1.0000	1.0000	1.0000
ψ_2 / ψ_1	0.9879	0.9970	0.9999
ψ_3 / ψ_1	0.9709	0.9909	0.9997
p	1.3047	2.7101	0.2346
e_{ext}^{21}	0.0065	0.2861	0.2033
GCI_{fine}^{21}	0.037	0.0036	0.0025

Fig. 3. Flowchart of the optimization design.

590000 nodes for the diffuser vane. To analyze the phenomena occurring near the wall region and to satisfy the shear stress transport reattachment modification turbulence (k-ω SST) model, the grid was refined with y^+ values less than 2 at all walls.

Previous researchers have numerically analyzed the internal flows of various hydraulic machines and experimentally verified the numerical scheme and techniques of the GCI method [29-31].

The flow description and turbulence analysis in the axial flow pump were based on the 3-D steady-state Reynolds-averaged Navier-Stokes (RANS) equations. In addition, the governing equations were discretized by the finite volume method. To improve the predictive ability of reattaching boundary layers, the k-ω SST model [32] was selected as the turbulence model. The k-ω turbulence model simulated the phenomena in the near-wall surface region while the k-ε turbulence model modeled the bulk region.

The single-phase water at 25 °C was employed as the working fluid. All walls (blades, hub and shroud) were adiabatic and no-slip. The impeller was the rotating domain and the inlet guide vane and diffuser vane constituted the stationary domain. To save time and computer resources, periodic conditions were applied on either sides of the channel. The stage model (mixing plane) was utilized at the interfaces between the stationary and rotational domains. The total pressure and mass flow rate were set at the inlet and outlet of the pump, respectively. Convergence was concluded when the performance parameters (such as efficiency, pressure head, and mass flow rate) fluctuated by less than 0.5 % during 100 time steps.

4. Multi-objective optimization

The optimal design for the multi-objective function used in this study was defined as follows.

Maximize: $\mathbf{F(x)} = [F_1(\mathbf{x}), F_2(\mathbf{x})]$
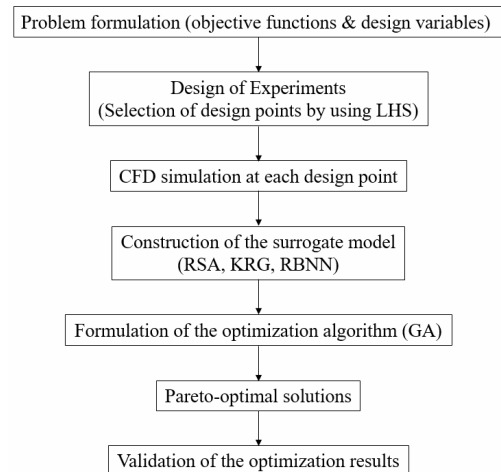Design variable bound: $\mathbf{LB} \leq \mathbf{x} \leq \mathbf{UB}, \mathbf{x} \in \mathbf{R},$

1. All objective functions are set to search for the maximum value, and 2. The range of each design variable is a real number and must exist within the upper and lower bounds [33].

Fig. 3 is a flowchart of the optimal design used in this study. As mentioned above, the first step in optimal design is to define the optimal problem and set the design goals.

The next step is to select design variables. Depending on the design target, the design variables are finite or infinite. In the case of the axial flow pump that is the subject of this study, it is impossible to consider all the design variables because there are countless design variables. Therefore, it is necessary to adopt a reasonable number of design variables by utilizing a screening technique. In this study, 2k factorial analysis was used to select design variables. The range of the chosen design variables was selected in consideration of pump manufacturing, and the design space was established through Latin hypercube sampling (LHS) [34], one of the design of experiment (DOE) methods.

Objective function values from each sample point derived through LHS are calculated through RANS, and a surrogate model is constructed using these values.

The final step is to derive Pareto-optimal solutions for multiple objective functions using genetic algorithms within the combined surrogate model using in-house code utilizing MATLAB R2018b [35].

4.1 RSA

The RSA model is generally a polynomial model based on regression prediction that depicts the continuous response **y** as a linear combination of a function of the predictor variable **x** and the random error ε [36], as shown in Eq. (5) below.

$$y = \sum_{j=1}^{N} \beta_j f_j (x) + \varepsilon, \ E(\varepsilon) = 0, \ V(\varepsilon) = \sigma^2 . \tag{5}$$

In the above equation, **x** is a vector representing a design

variable, $f_j(x)$ are the terms of the model, and β_j are the coefficients derived through the regression equation. It is assumed that the error ε is uncorrelated, the mean $\boldsymbol{E}$ is equal to 0, and the variance $\boldsymbol{V}$ is constant. In this study, a second-order polynomial RSA model was used, and it is expressed as follows.

$$y(x) = \beta_0 + \sum_{i=1}^{N} \beta_i x_i + \sum_{i=1}^{N} \beta_{ii} x_i^2 + \sum_{i<j}^{N} \beta_{ij} x_i x_j . \tag{6}$$

The goodness of fit was determined by the R_{adj}^2 value. For a good fit, R_{adj}^2 must be close to 1 [36].

4.2 KRG

The KRG model is a technique for constructing a predictive model using an interpolation method using a Gaussian random function [37]. That is, it is a technique for predicting by interpolating empty spaces within the design space based on sample data, and is expressed as the following function:

$$y(x) = \mu + D(x) . \tag{7}$$

In the above equation, x is a vector representing a design variable, μ is a constant global model and $D(x)$ denotes the local deviations from the global model (μ). As mentioned above, in the KRG model, local deviations at unknown points (regions excluding sample data) within the design space are expressed as a stochastic processes [37].

4.3 RBNN

The RBNN model [38] is a two-layer network configured to transform the hidden layer composed of radial basis neurons into a linear neuron output layer. It is characterized in that the network is divided into the input and output sets. The input set constitutes a non-linear hidden layer through a radial basis function, and the output set is derived using a linear combiner. The transfer function of the radial basis neuron used this work is a Gaussian function and is defined as follows:

$$radbas(n) = e^{-n^2} . \tag{8}$$

The predictive accuracy or ability of the neural network is stored in the weights obtained from the training pattern set, and the network training proceeds in the direction of minimizing the cross-validation (CV) error, and the training proceeds by changing the spread constant (SC) and the error target. The K-fold cross-validation (K-fold CV) method, used in this work, is performed as follows.

The data sample is divided into K separate subsets. The K-1 fold is used to train the neural network, and the other fold is used to compare the relative error with the predicted model (trained model). This process is repeated K times to calculate

the sum of relative errors as described in Eq. (9), and the neuron network is trained while changing the SC value.

$$CV(SC) = \frac{1}{K} \sum_{i=1}^{k} \in_k ; \in_k = \sum_{j=k^{th}\,set} (y_j - \hat{y}_j)^2 . \tag{9}$$

4.4 Genetic algorithm (GA)

GA is an algorithm implemented with inspiration from the evolutionary process of living things in nature [39]. Like other evolutionary algorithms, GA starts the search based on a randomly generated population. At each step of the search, the GA randomly extracts data to select the next generation of individuals within the current population. At this stage, the next generation is determined through three operators: selection, crossover, and mutation.

The "selection" operator creates a parent for the next generation. The "mutation" operator serves to ensure that the direction of evolution is not biased and prevents the algorithm from getting stuck in the local optima. Finally, the "crossover" operator acts as a filter passing the desired functionality from the current generation to the next.

5. Results and discussion

5.1 Impeller optimization

The pump hydraulic performance was optimized by maximizing the objective functions, namely, the total head and total efficiency, which are respectively defined as follows:

$$H_t = \frac{P_{outlet} - P_{inlet}}{\rho g} \tag{10}$$

$$\eta = \frac{\rho g H Q}{\zeta . \omega} . 100\% \tag{11}$$

here P_{outlet} and P_{inlet} denote the total pressures at the outlet and inlet, respectively, and ρ, ζ and ω are the water density, torque of impeller and hub, and angular velocity of impeller, respectively.

The hydraulic performance of the axial pump depends on numerous parameters of the impeller, such as the meridional impeller length, inlet and outlet blade angles, hub ratio, setting angle, and sweep angle. To reduce the number of experiments for impeller optimization, the factors that majorly affect the objective functions were determined in a 2^k factorial-design analysis [40]. This method is widely utilized in experiments with two levels of k factors: the k main effects and the interactions between 2 factors, 3 factors… k factors. If there are many factors, the total number of runs in a 2^k full factorial design is very large. To conserve computational time and cost, the present study performs a fractional factorial-design analysis rather than a full 2^k factorial-design analysis. As its name suggests, the fractional factorial design considers only a fraction of all possi-
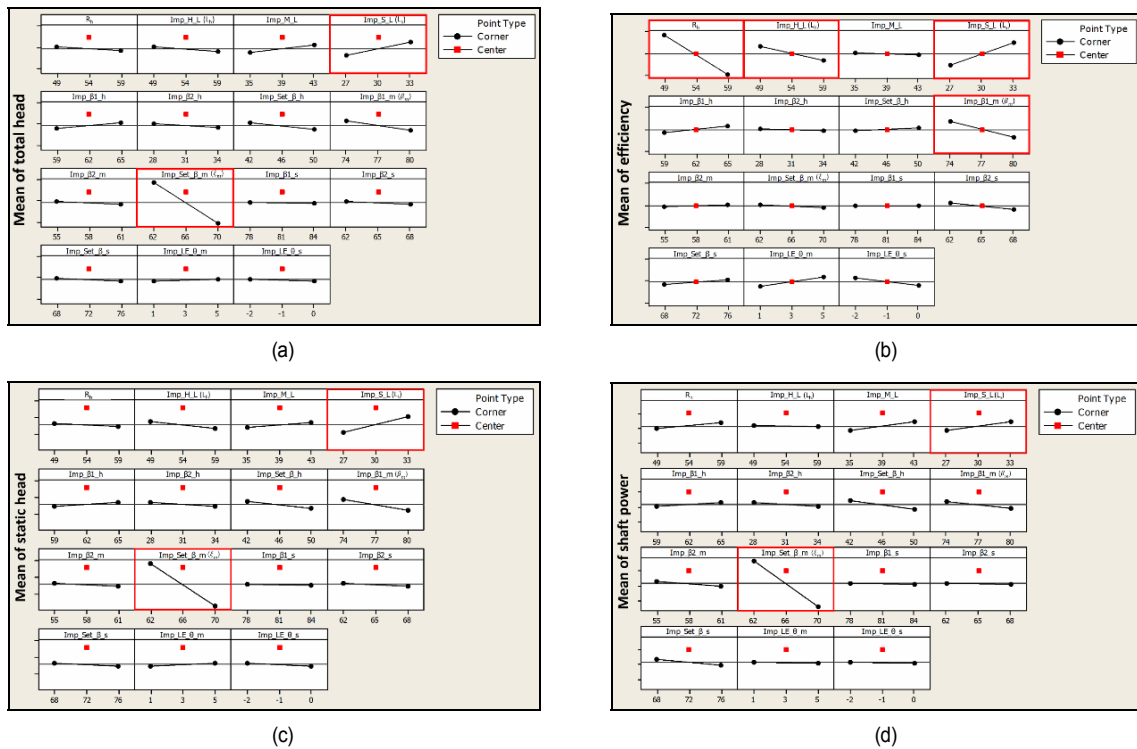
Fig. 4. Effects of impeller design parameters on (a) total head; (b) efficiency; (c) static head; (d) shaft power of the pump. The main influencing parameters are outlined in red.
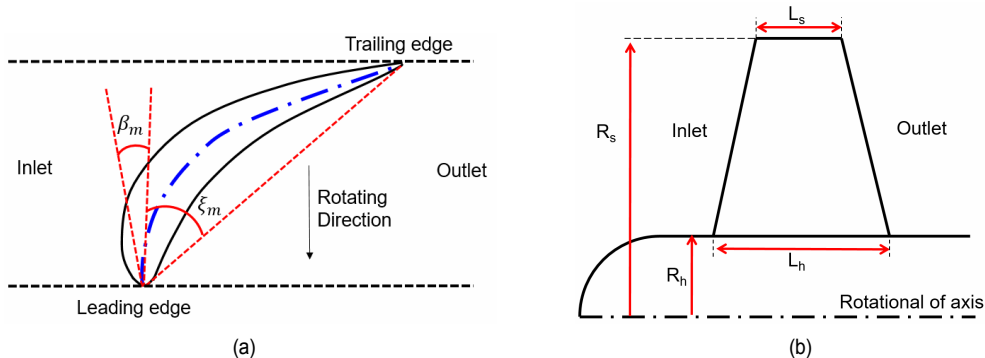

Fig. 5. Design variables of the impeller on the (a) blade-to-blade plane; (b) meridional plane, L_s: shroud chord length; L_h: hub chord length; R_h: hub radius; R_s: shroud radius; ξ_m: stagger angle at mid span; β_m: inlet blade angle at mid span.

ble treatment combinations. It also uses resources more efficiently than the full factorial design because it decreases the sample size of an experiment. Therefore, fractional factorial designs lower the number of required combinations in screening experiments.

In the factorial design of the impeller optimization, 15 factors were considered at level IV resolution. The total number of 2^k factorial design sets was 32. The effects of the impeller design parameters on the total head, total efficiency, static head, and shaft power are presented in Fig. 4. Red color boxes present the main factors that affected the hydraulic performance of the pump. For total head, static head and shaft power, shroud chord length (L_s) and stagger angle at mid span (ζ_m) are main influencing factors. The total efficiency was dominantly contrib-

uted by four parameters: hub ratio (R_r), hub chord length (L_h), L_s, and inlet blade angle at mid span (β_m). Therefore, over a wide range of design parameters, the hydraulic performance was mainly affected by R_r, L_s, L_h, β_m, and ζ_m. The design variables are shown in Fig. 5. The hub ratio is defined to be the same as the impeller diameter ratio, where the shroud diameter is fixed and the hub diameter is variable. Besides affecting the efficiency of the pump, R_r directly affected the structure of the rotating shaft. Therefore, it was adjusted to meet the point of highest performance at hub ratio of 0.2432.

After screening through the 2^k factorial design analysis, the DOE was implemented by LHS, which chooses random sample points in the design space. The parameter values selected by LHS are well distributed over the design space. Being

Table 3. Design space of impeller optimization.

Variable	ΔL_s (mm)	ΔL_h (mm)	$\Delta \xi_m$ (Deg.)	$\Delta \beta_m$ (Deg.)
Lower bound	0	−10	−4	−3
Upper bound	+6	0	+4	+3
Reference	0	0	0	0
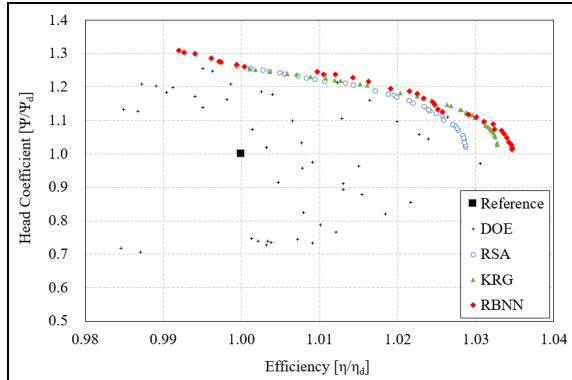
Fig. 6. Pareto optimal solutions of the impeller optimization.

Table 4. Design variables of the impeller optimization.

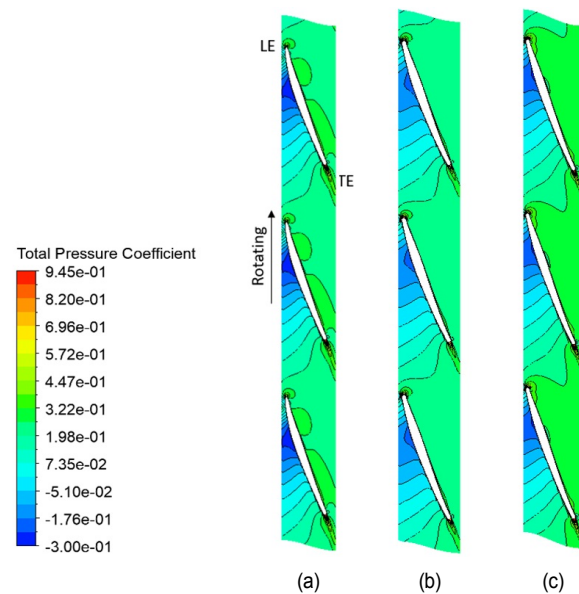| Approximation model	L_s	L_h	ξ_m	β_m
RSA 1	+5.994	−5.917	−0.417	−2.769
RSA 2	+5.978	−2.88	−2.251	−2.639
RSA 3	+5.932	−1.091	−3.647	+2.168
RSA 4	+5.154	−2.927	−3.435	+1.647
KRG 1	+5.958	−4.24	−0.463	+0.121
KRG 2	+5.965	−3.254	−2.723	+0.02
KRG 3	+5.856	−0.982	−3.853	+0.023
KRG 4	+5.543	−3.901	−3.439	+0.937
RBNN 1	+5.447	−5.461	−0.217	+0.226
RBNN 2	+4.925	−1.289	−2.749	−1.616
RBNN 3	+5.831	−5.377	−3.665	+2.89
RBNN 4	+5.052	−2.555	−3.28	−1.664

Fig. 7. Total pressure coefficient contours at 90 % span of the impeller in (a) the reference model; (b) the changed hub-ratio model; (c) the optimum model.

based on the Latin square design, LHS takes one sample in each column and each row. LHS is widely used in design-point selection because it can significantly decrease the required number of runs to obtain a reasonable result. Table 3 specifies the range of design variables in the impeller optimization. Forty-eight design points within the design space were selected by LHS and the relationships between the design variables and objective functions were then identified.

In this study, the values of the objective functions were predicted by three basic surrogate models (RSA, KRG, and RBNN). Fig. 6 shows the Pareto optimal solutions (POSs) of the impeller optimization. Because the total pressure head and total efficiency were simultaneously optimized, increasing (decreasing) the total pressure decreased (increased) the total efficiency.

Representative Pareto-optimal designs for the simulations (see Table 4) were derived from the POSs by K-means clustering [41]. Each approximation model performed three multi-objective optimizations followed by one single-objective optimization under the design constraints. In the single-objective optimization, the objective function was the total efficiency and the constraint condition was the total head ($\psi / \psi_d > 1.216$).

The hydraulic performances of the impeller design models in Table 4 are listed in Table 5. Both the total efficiency and total head were higher in the optimized models than in the reference model. The efficiency and total pressure head were improved by a maximum of 2.6 % and 24.6 %, respectively. In addition, the RSA model minimized the prediction error. Compared to the reference design, the KRG 3 model maximized the total pressure head but minimally increased the total efficiency among the optimized models. In contrast, the RSA 1 and RBNN 1 models achieved the highest total efficiency but minimally increased the total pressure head among the optimized

models. The RBNN 4 model was selected as the optimal model that best balanced the total efficiency versus total pressure head tradeoff. The total efficiency and total pressure head were 0.97 % and 21.03 % higher, respectively, in RBNN 4 than in the reference model.

To evaluate the effect of shroud chord length (L_s), Fig. 7 plots the total pressure coefficient (C_p) contours at 90 % span of the impeller in the reference model, the changed hub-ratio design, and the optimum design. In the reference model, the total pressure was unevenly distributed at the pressure side of the impeller and a widely distributed low-pressure region appeared along the blade passage. After changing the hub diameter, the increased cross-sectional area significantly decreased the total pressure at the pressure side of the impeller, but the total pressure was notably increased near the leading edge (LE) on the

Table 5. Hydraulic performances of the impeller optimization.

| Design model	Predicted values		RANS analysis		Prediction error (%)		Increment (%)	
	η / η_d	Ψ / Ψ_d	η / η_d	Ψ / Ψ_d	η	Ψ	η	Ψ
Reference	-	-	1.000	1.000	-	-	-	-
RSA 1	1.027	1.071	1.026	1.072	0.160	0.108	2.566	7.237
RSA 2	1.019	1.175	1.019	1.175	0.036	0.010	1.900	17.473
RSA 3	1.004	1.243	1.004	1.240	0.017	0.205	0.440	24.039
RSA 4	1.005	>1.216	1.008	1.197	0.295	-	0.834	19.697
KRG 1	1.030	1.089	1.025	1.087	0.513	0.160	2.520	8.696
KRG 2	1.017	1.195	1.014	1.193	0.361	0.145	1.380	19.349
KRG 3	1.004	1.244	1.002	1.246	0.215	0.121	0.203	24.560
KRG 4	1.011	>1.216	1.008	1.214	0.328	-	0.774	21.376
RBNN 1	1.032	1.064	1.026	1.066	0.618	0.120	2.606	6.554
RBNN 2	1.018	1.198	1.013	1.196	0.514	0.155	1.270	19.627
RBNN 3	0.996	1.284	1.006	1.215	0.991	5.436	0.603	21.457
RBNN 4	1.014	>1.216	1.010	1.210	0.446	-	0.974	21.028
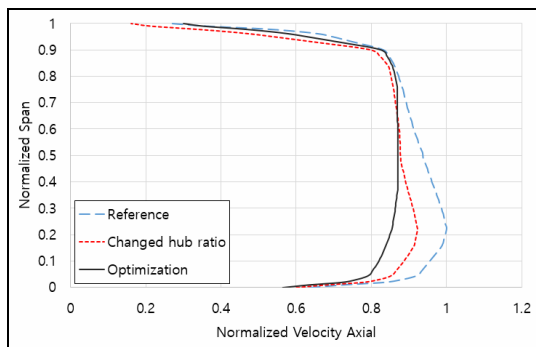
Fig. 8. Velocity axial distributions in spanwise direction at the impeller outlet.

suction side of the impeller. In the optimized design, the low-pressure regions in the passage were greatly improved because the total pressure was more evenly distributed at the pressure side of the impeller than in the reference model. The C_p was calculated as:

$$C_P = \frac{P - P_{in}}{\frac{1}{2}\rho V^2} \qquad (12)$$

where P, P_{in} and V are the total pressure in the stationary frame, the averaged total pressure at the inlet in the stationary frame, and the velocity at the impeller tip, respectively.

Fig. 8 compares the normalized axial-velocity distributions in spanwise direction at the impeller outlet in the reference model, changed hub-ratio design, and optimum design. The normalization factor was the maximum velocity of the reference case. Because the cross-sectional area of the impeller chamber was enlarged in comparison with the reference model, the velocity distribution decreased from that in the reference design model at the same flow rate. The trends of axial velocity distributions

were very similar in the three cases. Near the hub and shroud (i.e. near the wall), the friction between the wall and flow was increased by viscosity effects, so the velocity decreased. In the reference model, the axial-velocity distribution was non-uniform, indicating a sharp velocity increase to near 20 % span, then a gradual decrease with increasing span before dropping at 90 % span. The same tendency but with slight improvements was observed in the changed hub-ratio model. After optimization, the axial velocity distribution was stabilized and was significantly improved around the 20 % span from that of the reference design.

Fig. 9 compares the pressure distributions of the impeller in the streamwise direction in the reference design, changed hub-ratio design, and optimum design at 10 % span, 50 % span and 90 % span. The pressure was normalized by the highest pressure in the reference case. In all three design models, the pressure increased sharply at the LE of the impeller because the stagnation point was located there. The pressure was also severely reduced at the LE, where the velocity was accelerated at both sides of the impeller. The pressure at the pressure side slightly decreased after changing the hub ratio. In the optimal design, the pressure distribution at the pressure side was restored to that of the reference model. In all three designs, the pressure distribution at the pressure side remained almost constant. At the suction side, the pressure at each streamwise position of the optimized model steadily increased from that of the reference design. This increase was attributed to the change in hub radius, which caused the velocity reduction.
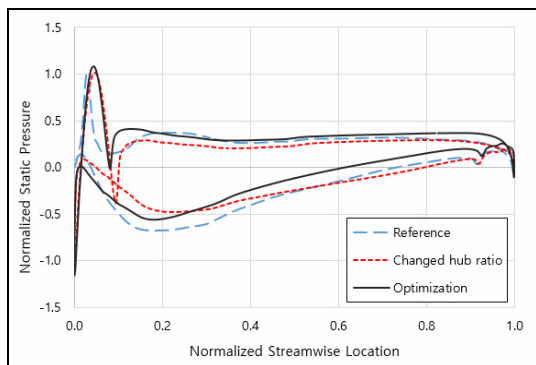
Fig. 10 plots the static and total pressure distributions at 50 % span of the impeller in the three designs. The pressure was normalized by the highest pressure in the reference case. Both the static and total pressures increased with increasing streamwise location. As the streamwise position increased from 10 % to 80 %, the pressure increased sharply because the fluid received dynamic energy from the rotating blade. Out
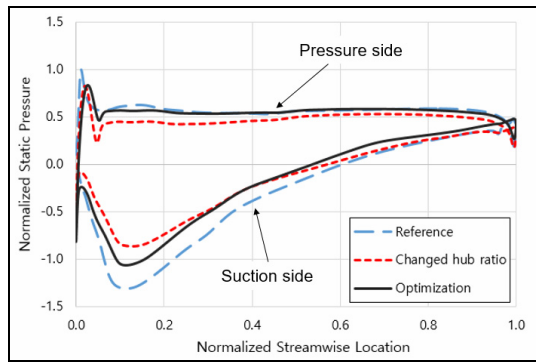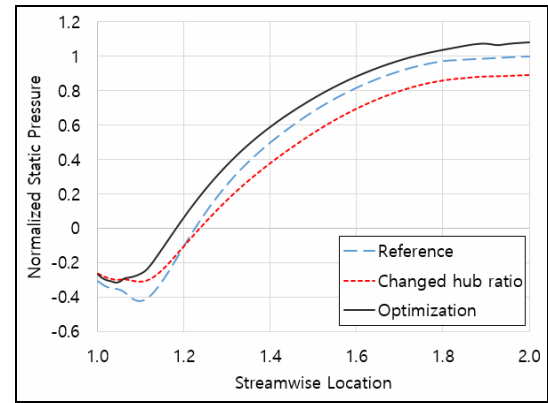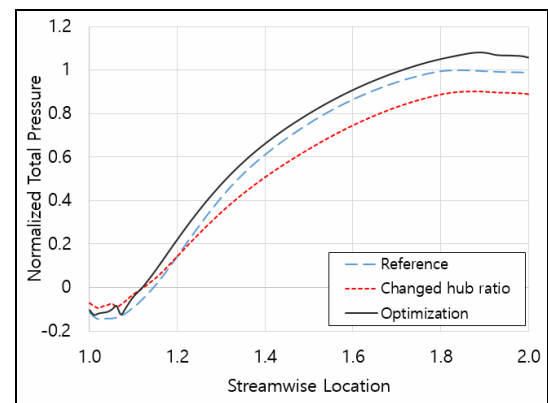
(a)
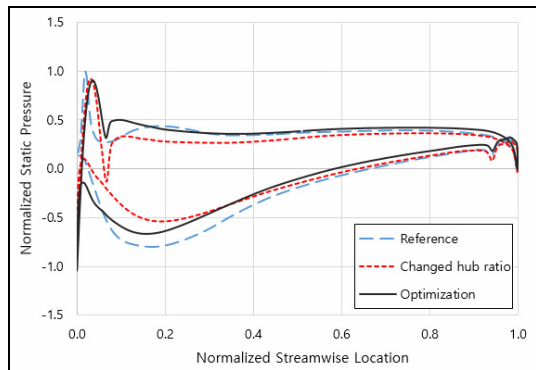
(b)

(c)

Fig. 9. Blade loading distributions of the impeller at: (a) 10 % span; (b) 50 % span; (c) 90 % span.

(a)

(b)

Fig. 10. Static (a); total (b) pressure distributions in the three models at 50 % span.

side of this region, where the impeller was absent, the pressure was almost unchanged. The static and total pressure distributions exhibited the same trends, indicating that the total pressure was mainly enhanced by the increase in static pressure. After decreasing the hub diameter, the cross-sectional area was increased and the torque was 12.812 % lower than in the original model. Accordingly, the pressure was lower than in the reference case. However, after optimization, the improved shape of the impeller blade enhanced the torque by 4.564 % from that of the reference model and caused a slight increase in pressure. In the static pressure distribution of the reference case, the slight pressure drop at streamwise positions around 10 % suggests the formation of a low-pressure region in front of the LE of the impeller. This phenomenon was improved after changing the radius of the hub.
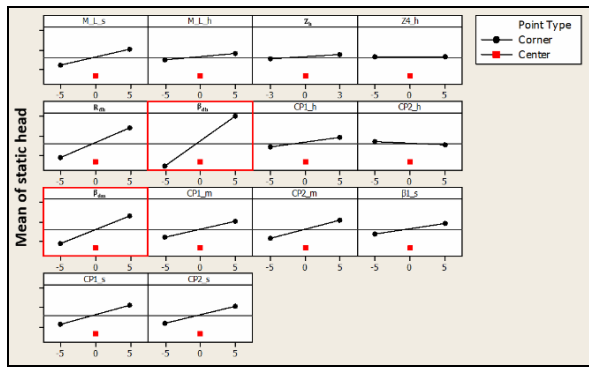
5.2 Diffuser optimization

In multi-objective optimization of the diffuser vane, the objective functions were the total efficiency and total pressure head calculated by Eqs. (10) and (11), respectively. Many parameters of the diffuser-vane size affect the hydraulic performance of the axial flow pump, including (but not limited to) the shroud and hub meridional lengths of the diffuser (L_{ds} and L_{dh}, respectively) and the inlet and outlet blade angles. In this part, fourteen factors were screened through a 2^k factorial design analysis with 32 design sets. The red boxes in Fig. 11 highlight the main design variables affecting the hydraulic performance of the axial pump. The total and static heads were mainly influenced by the hub-blade and middle-blade angles at the LE (β_{dh} and β_{dm}, respectively). The total efficiency was affected by two parameters: the hub radius at the trailing edge (R_{dh}) and β_{dh}. In addition, the hub position at the LE (Z_h) and β_{dh} influenced the shaft power. In summary, the four main design parameters influencing the hydraulic performance were R_{dh}, Z_h, β_{dh} and β_{dm}. Here, the blade angle at the LE (β_d) is the angle between the tangent of the camber line and the axis of rotation. These de-
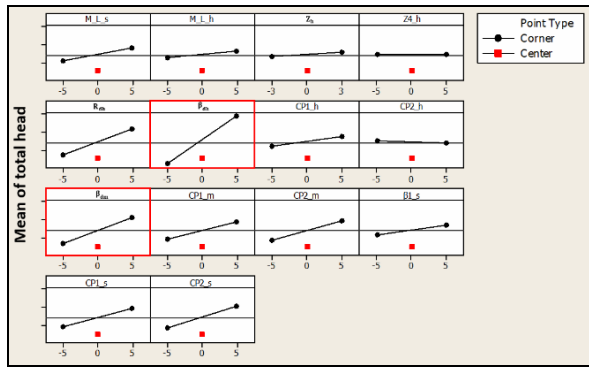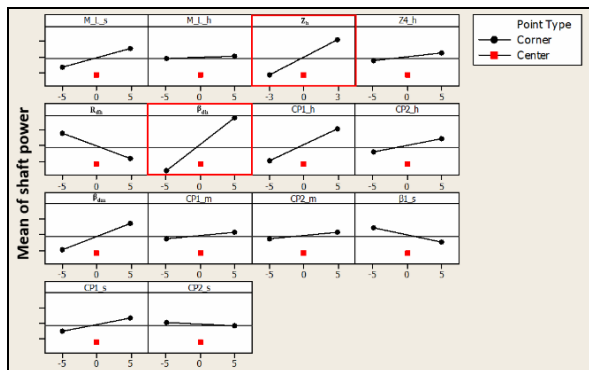
(a)
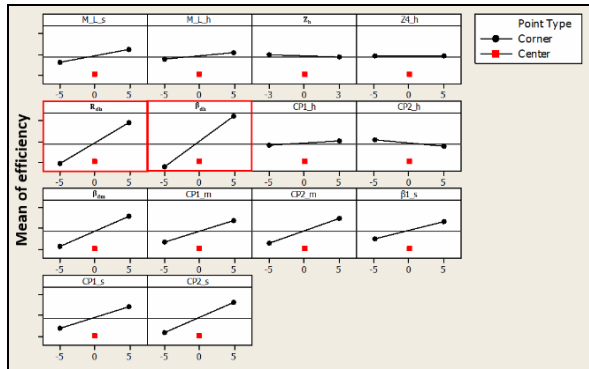
(b)

(c)

(d)

Fig. 11. Effects of diffuser-vane design parameters on (a) total head; (b) efficiency; (c) static head; (d) shaft power of the pump. The main influencing parameters are outlined in red.

Table 6. Design space of the diffuser vane optimization.

Variable	$\Delta\beta_{dh}$ (Deg.)	$\Delta\beta_{dm}$ (Deg.)	ΔZ_h (mm)	ΔR_{dh} (mm)
Lower	0	0	0	0
Upper	+10	+10	+3	+10
Reference	0	0	0	0

Table 7. Design variables of the impeller optimization.

| Approximation model	B_{dh}	B_{dh}	Z_h	R_{dh}
RSA 5	+9.99986	+9.952248	+0.002126	+7.254067
RSA 6	+9.999865	+9.260224	+0.001441	+7.255352
RSA 7	+9.99987	+7.241996	+0.000928	+7.289964
KRG 5	+10.000	+0.005586	+1.609147	+6.22488
KRG 6	+10.000	+0.007593	+2.058225	+7.083937
KRG 7	+10.000	+0.007125	+1.834994	+6.572676
RBNN 5	+10.000	+5.201492	+2.999934	+3.38999
RBNN 6	+10.000	+5.282597	+2.999926	+3.104141
RBNN 7	+10.000	+5.074965	+2.999958	+3.737709

(a)

(b)
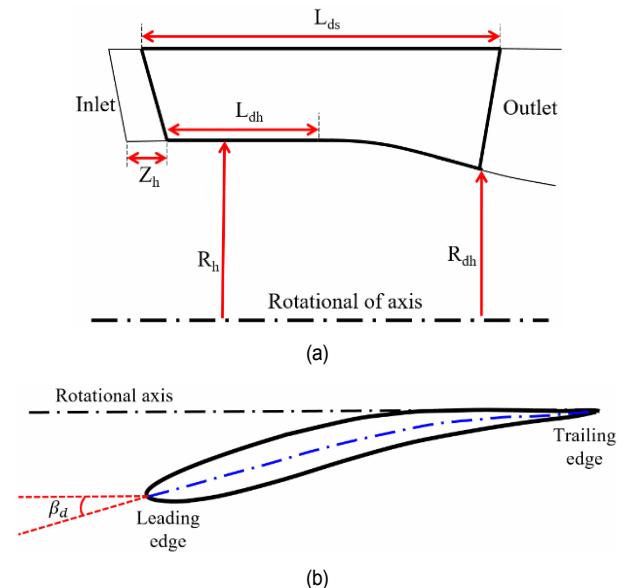
Fig. 12. Design variables of the diffuser vane on the (a) meridional plane; (b) blade-to- blade plane. L_{ds}: shroud meridional length of the diffuser; L_{dh}: hub meridional length of the diffuser; R_{dh}: hub radius at the trailing edge; Z_h: hub position at the leading edge; β_d: hub-blade angle at the leading edge.

sign variables are geometrically defined in Fig. 12.

Sample points within the design space were randomly selected by LHS with four design variables. The ranges for the design variables in the diffuser vane optimization are given in Table 6. Forty-eight design points were created in the design space for identifying the relationship between these variables and the objective functions.

Again, the objective function values were predicted using the RSA, KRG, and RBNN surrogate models. Tables 7 and 8 list

Table 8. Hydraulic performances of the diffuser-vane optimization.

| Design model	Predicted values		RANS analysis		Prediction error (%)		Increment (%)	
	η / η_d	Ψ / Ψ_d	η / η_d	Ψ / Ψ_d	η	Ψ	η	Ψ
Reference	-	-	1	1	-	-	-	-
RSA 5	1.032	1.101	1.031	1.102	0.130	0.121	3.097	10.205
RSA 6	1.031	1.101	1.028	1.098	0.325	0.280	2.802	9.805
RSA 7	1.029	1.102	1.022	1.071	0.666	2.786	2.224	7.115
KRG 5	1.028	1.092	1.013	1.087	1.408	0.442	1.344	8.727
KRG 6	1.026	1.095	1.005	1.075	2.022	1.837	0.517	7.536
KRG 7	1.027	1.094	1.007	1.063	1.999	2.806	0.657	6.335
RBNN 5	1.055	1.132	1.017	1.099	3.656	2.956	1.672	9.867
RBNN 6	1.055	1.132	1.010	1.071	4.331	5.344	0.978	7.115
RBNN 7	1.055	1.132	1.009	1.076	4.379	4.978	0.865	7.598
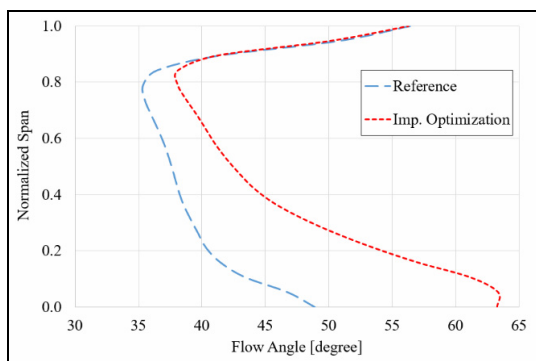
Fig. 13. Comparisons of flow angles at the leading edge of the diffuser vane in the reference and optimized models.
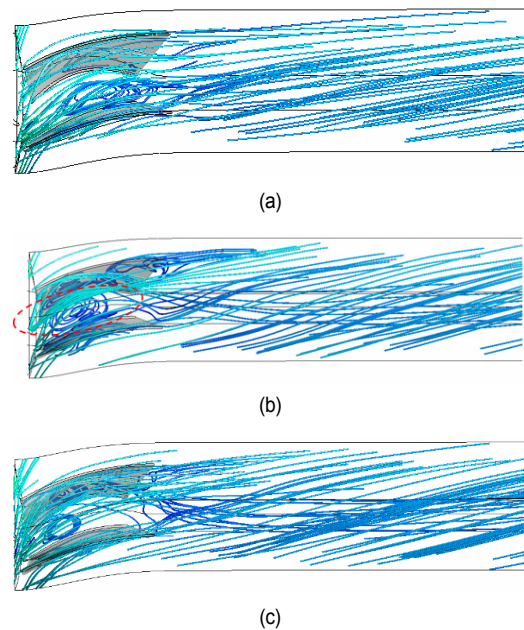

(a)

(b)

(c)

Fig. 14. Velocity streamline distributions in the passage of the diffuser vane in the (a) reference; (b) optimized impeller; (c) optimized diffuser vane models.

the design variable values and objective function values, respectively. Multi-objective optimizations without any constraint conditions are applied in the diffuser vane optimization.

The total efficiencies and total pressure heads were higher in the approximation models than in the reference model, with minimum enhancements of 0.517 % in total efficiency and 6.335 % in total pressure head. The prediction errors in the diffuser vane optimization were minimized in the RSA models. The optimized RSA 5 model achieved the highest increase in total efficiency (3.097 %) relative to the reference model. This approximation model also maximized the total head (10.205 % above that of the reference model) and minimized the difference between the predicted value and the RANS analysis value of the objective functions. Therefore, RSA 5 was selected as the optimal design for the diffuser vane.

Fig. 13 compares the velocity flow angles at the LE of the diffuser vane in the models with the original and optimized (RBNN 4) impellers. The angle between the blade-to-blade velocity and circumferential velocity vector components is known as the velocity flow angle. The impeller optimization largely changed the flow direction. The velocity flow angles in the two cases were almost identical near the shroud, but from 80 % span onward, the flow angles gradually diverged with

decreasing span. When the difference reached its maximum (40.83 %), the mismatched blade and flow angles caused large vortex activity in the diffuser vane passage (see Fig. 14(b)). The vortex formed at the inlet of the diffuser vane blocked the flow and prevented its smooth exit, resulting in large hydraulic losses. Therefore, impeller optimization of the full component model reduced the total efficiency by 8.04 % from that of the reference case. After optimizing the diffuser vane, the vortex in the diffuser vane passage was notably improved (Fig. 14(c)) and the hydraulic performance of the axial flow pump was improved accordingly. Therefore, the hydraulic performance was enhanced through elimination of the vortex appearing in the diffuser vane passage.

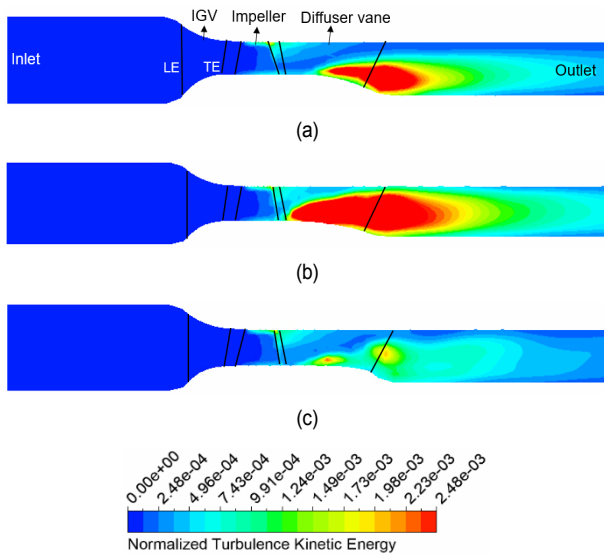To clarify the turbulence intensity of the flow in the diffuser

Fig. 15. Normalized turbulence kinetic energy distributions on the meridional plane in the (a) reference; (b) optimized impeller; (c) optimized diffuser vane models.
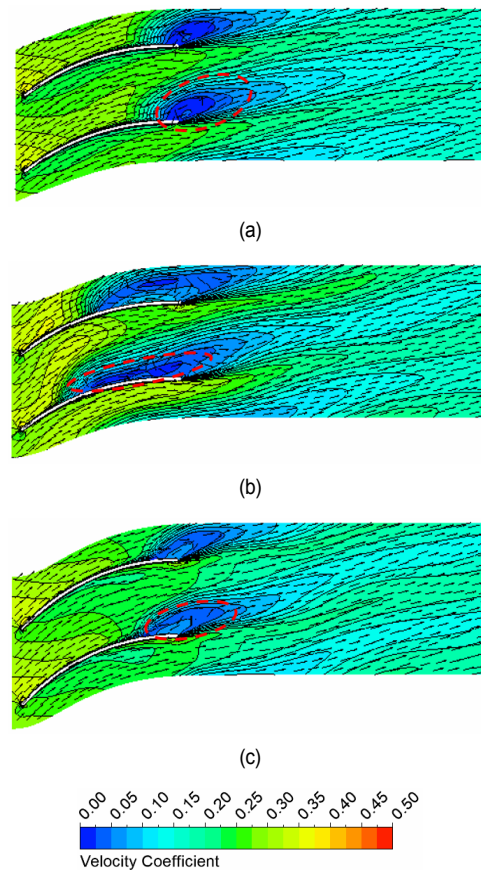

Fig. 16. Velocity coefficient contours (colors) and vector distributions (quiver plots) at the mid-plane of the diffuser vane in the (a) reference; (b) optimized impeller; (c) optimized diffuser vane models.

Fig. 17. Static pressure coefficient distributions in the meridional planes in the (a) reference; (b) optimized impeller; (c) optimized diffuser vane models.

vane passage, Fig. 15 displays the normalized turbulence kinetic energy (TKE) distributions along the meridional plane in the reference, optimized impeller, and optimized diffuser vane models. The TKE was normalized by the square of the velocity at the impeller tip. In the reference design, vortex formation increased the TKE value near the hub of the diffuser vane. In the optimized impeller model (Fig. 15(b)), the flow and blade angles were incompatible and the fluid approached the diffuser vane at a high incidence angle, causing flow separation at the LE of the diffuser vane. Consequently, vortices formed on the suction side and widely spread through the diffuser passage, raising the TKE and seriously degrading the hydraulic performance. After optimizing the diffuser vane, this phenomenon was greatly diminished by vortex suppression in the passage. Therefore, the total efficiency and total pressure head were significantly increased in the optimized diffuser-vane model.

Fig. 16 depicts the velocity coefficient contours and velocity vector distributions at 50 % span of the diffuser vane in the three cases. The velocity coefficient defines the velocity as a ratio of the velocity at the tip of the impeller. A high-velocity zone appeared near the LE on the suction side of the diffuser vane. In the reference case, the velocity at the trailing edge (TE) of the diffuser vane was reduced by small vortex formations (Fig. 16(a)). After optimizing the impeller, many vortices formed at the suction side of the diffuser vane, caused by flow separation from the blade surface (Fig. 16(b)). This vortex formation created a large low-velocity zone extending from the middle of the blade to the TE of the diffuser vane. Within this zone, the flow tended to accelerate near the pressure side of the adjacent blade and the velocity distribution became uneven. After optimizing the diffuser vane, the low-velocity zone at the suction side was considerably improved (Fig. 16(c)). Only a small and weak low-velocity area formed at the TE of the dif-

(a)

(b)

(c)
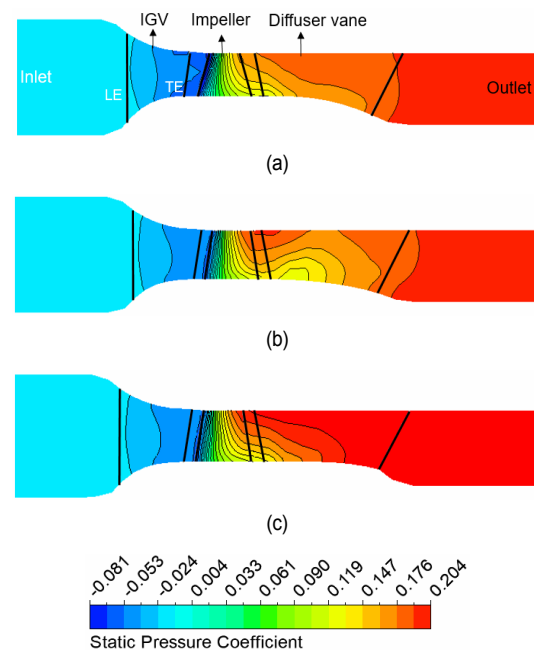
Fig. 18. Blade-loading distribution of the diffuser vane at different spans: (a) 10 %; (b) 50 %; (c) 90 %.

Fig. 19. Hydraulic performance characteristics of the axial flow pump in the reference and optimized models.

fuser vane. The velocity distribution gradually reduced from the LE to the TE and the distribution also become more uniform in the diffuser vane passage.
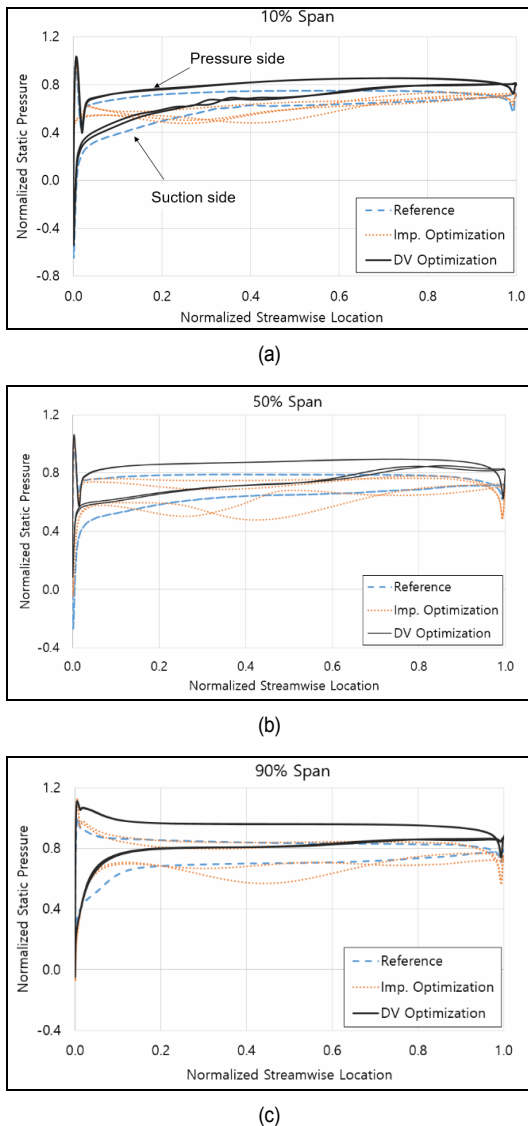
Fig. 17 compares the static pressure coefficient distributions on the meridional plane in the optimized and reference designs. The static pressure coefficients were calculated by Eq. (12), where P and P_{in} are static pressures. In the reference model (Fig. 17(a)), the pressure distribution was non-uniform at the LE of the impeller because a low-pressure zone formed there. This low-pressure zone can cause bubble formation and cavitation at the LE of the impeller. In the optimized impeller model (Fig. 17(b)), the low- pressure area at the LE of the impeller was eliminated but a non-uniform pressure distribution appeared in the diffuser vane region. The static pressure was negligibly increased in the low-pressure zone caused by vortex formation in the diffuser vane, leading to serious losses in hydraulic performance. After optimizing the diffuser vane (Fig.
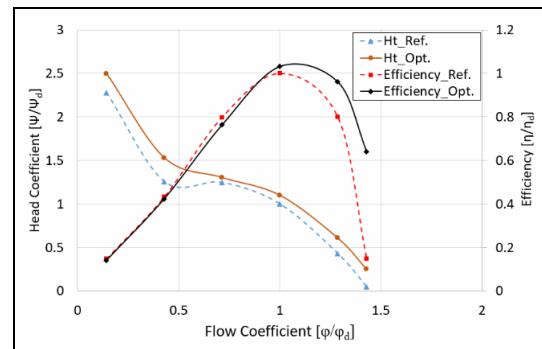
17(c)), the vortex flow was suppressed and the static pressure was significantly increased. The pressure distribution became more uniform and was gradually enhanced along the inlet-to-outlet direction of the axial flow pump.

Fig. 18 compares the pressure distributions of the diffuser vane in the streamwise direction in the reference, optimized impeller, and optimized diffuser-vane designs at different spans (10 %, 50 %, and 90 %). The pressure was normalized by the highest static pressure in the reference case. A high-pressure peak appeared at the LE of the diffuser vane of all designs and was attributed to the stagnation point. The static pressures clearly differed among the three cases. The pressure distribution in the reference case was stable at each streamwise location. In the optimized impeller case, the pressure distribution was non-uniform along the diffuser vane surface. This instability was caused by vortex formations at normalized streamwise positions 0.2-0.6 in the diffuser vane passage. After optimizing the diffuser vane, the static pressure notably increased because the vortices in the diffuser vane passage were eliminated.

Fig. 19 shows the hydraulic performance characteristics of the axial flow pumps in the reference and optimized design cases. The hydraulic performance was significantly higher in the optimized design than in the reference design, although the total efficiency was unchanged (φ / φ_d < 1.0). However, when the flow rate exceeded the design flow rate, the total efficiency increased sharply in the optimized design. At each flow rate, the total head was clearly enhanced from that of the reference design, especially in the saddle zone [42] at $0.5\,\varphi / \varphi_d$. The increase in hydraulic performance was mainly attributed to the increased inflow at the impeller and vortex suppression in the diffuser passage.

6. Conclusions

In this study, the impeller and diffuser vane of an axial flow pump were optimized by multi-objective optimization. The objective functions were the total efficiency and total head. The main influencing factors were screened through a 2^k factorial design analysis and the design points were then created in the

design space using Latin hypercube sampling. In each optimization process, the optimal design was found using three surrogate models (RSA, KRG, RBNN).

In the first optimization, the impeller was optimized with four design variables. The RBNN 4 model was chosen as the optimum design which enhanced the total efficiency and total pressure head by 0.974 % and 21.028 %, respectively, from those of the original impeller. The hydraulic performance was significantly enhanced by redistribution of the velocity field at the outlet and low-pressure suppression in front of the impeller. After optimizing the impeller, the diffuser vane was optimized (again with four design variables). The RSA 5 model was selected as the optimum design because it maximized the objective function values while minimizing the predicted errors. The RSA 5 model improved the total efficiency and total head by 3.097 % and 10.205 %, respectively, from those of the reference design. The new diffuser vane improved the discordance between the flow and blade angles, thereby removing vortices from the diffuser vane passage and greatly increasing the total efficiency and total head. After optimizing the design, the hydraulic performance characteristics revealed a sharp increase in total efficiency in the high-flow-rate region. In addition, the total-head curve was smoother and higher-valued than in the reference design.

In future work, the reference and optimum models will be investigated and validated in experiments. The hydraulic performances will be investigated in prototype models and the characteristics of internal flow will be analyzed in more detail using the flow-visualization technique.

Acknowledgments

Nomenclature

n_a	: Specific speed
n	: Rotational speed
Q	: Flow rate
H	: Pressure head
H_t	: Total head
φ	: Flow rate coefficient
D	: Impeller diameter
ψ	: Head coefficient
ϕ	: Rotational speed coefficient
η	: Total efficiency
ζ	: Torque
ω	: Angular velocity
P_{outlet}	: Total pressure at outlet
P_{inlet}	: Total pressure at inlet
ρ	: Density of the water

g	: Gravitational acceleration
L_s	: Shroud chord length
ξ_m	: Stagger angle at mid span
R_h	: Radius of hub
L_h	: Hub chord length
β_m	: Inlet blade angle at mid span
C_p	: Pressure coefficient
P	: Pressure in stationary frame
P_{in}	: Averaged pressure in stationary frame at the inlet
V	: Velocity at tip of the impeller
L_{ds}	: Shroud meridional length of the diffuser
L_{dh}	: Hub meridional length of the diffuser
β_{dh}	: Hub blade angle at leading edge
β_{dm}	: Middle blade angle at leading edge
R_{dh}	: Hub radius at trailing edge
Z_h	: Hub position at leading edge
β_d	: Blade angle at leading edge
N_1, N_2, N_3	: Number of grid
r	: Grid refinement factor
p	: Apparent order

References

[1] P. Lin, M. Liu, W. Zhao, Z. Liu, Y. Wu, F. Xue and Y. Zhang, Influence of tip clearance on the performance of a screw axial-flow pump, *Advances in Mechanical Engineering*, 9 (6) (2017) 1-10.

[2] J. Feng, X. Luo, P. Guo and G. Wu, Influence of tip clearance on pressure fluctuations in an axial flow pump, *Journal of Mechanical Science and Technology*, 30 (4) (2016) 1603-1610.

[3] W. M. Feng, J. Y. Pan, Z. W. Guo and Q. Cheng, The effects of variable-inlet guide vanes on performance of an axial flow pump with tip clearance, *Proceedings of the ASME/JSME/KSME 2015 Joint Fluids Engineering Conference*, 1 (2015) 2015-33499.

[4] W. Han, Y. Liuy, C. Gongz and Y. Su, Effect of tip clearance on performance of contra-rotating axial flow water-jet propulsion pump, *Modern Physics Letters B*, 34 (10) (2020) 2050094.

[5] S. Shen, Z. Qian, B. Ji and R. K Agarwal, Numerical investigation of tip flow dynamics and main flow characteristics with varying tip clearance widths for an axial-flow pump, *Proc IMechE Part A: Journal of Power and Energy* (2018) 1-13.

[6] Y. S. Kim, M. W. Heo, H. S. Shim, B. S. Lee, D. H. Kim and K. Y. Kim, Hydrodynamic optimization for design of a submersible axial-flow pump with a swept impeller, *Energies*, 13 (12) (2020) 3053.

[7] J. W. Suh, J. W. Kim, Y. S. Choi, J. H. Kim, W. G. Joo and K. Y. Lee, Multi-objective optimization of the hydrodynamic performance of the second stage of a multi-phase pump, *Energies*, 10 (9) (2017) 1334.

[8] L. Shi, J. Zhu, F. Tang and C. Wang, Multi-disciplinary optimization design of axial-flow pump impellers based on the approximation model, *Energies*, 13 (4) (2020) 779.

[9] T. Mu, R. Zhang, H. Xu, Y. Zheng, Z. Fei and J. Li, Study on improvement of hydraulic performance and internal flow pat-

tern of the axial flow pump by groove flow control technology, *Renewable Energy*, 160 (2020) 756-769.

[10] J. Zhang, H. Zhu, C. Yang, Y. Li and H. Wei, Multi-objective shape optimization of helico-axial multiphase pump impeller based on NSGA-II and ANN, *Energy Conversion and Management*, 52 (1) (2011) 538-546.

[11] Y. Zhang, Y. Xu, Y. Zheng, E. F. Rodriguez, A. Sun, C. Yang and J. Wang, Multi-objective optimization design and experimental investigation on the axial flow pump with orthogonal test approach, *Complexity*, 2019 (2019) 1-14.

[12] F. Meng, Y. Li, S. Yuan, W. Wang, Y. Zheng and M. Koranteng Osman, Multiobjective combination optimization of an impeller and diffuser in a reversible axial-flow pump based on a two-layer artificial neural network, *Processes*, 8 (3) (2020) 309.

[13] F. Miao, H. S. Park, C. Kim and S. Ahn, Swarm intelligence based on modified PSO algorithm for the optimization of axialflow pump impeller, *Journal of Mechanical Science and Technology*, 29 (11) (2015) 4867-4876.

[14] I. S. Jung, W. H. Jung, S. H. Baek and S. Kang, Shape optimization of impeller blades for a bidirectional axial flow pump using polynomial surrogate model, *International Journal of Mechanical and Mechatronics Engineering*, 6 (6) (2012) 1097-1103.

[15] W. Wang, Y. Li, M. K. Osman, S. Yuan, B. Zhang and J. Liu, Multi-condition optimization of cavitation performance on a double-suction centrifugal pump based on ANN and NSGA-II, *Processes*, 8 (9) (2020) 1124.

[16] K. Wang, G. Luo, Y. Li, R. Xia and H. Liu, Multi-condition optimization and experimental verification of impeller for a marine centrifugal pump, *International Journal of Naval Architecture and Ocean Engineering*, 12 (2020) 71-84.

[17] H. S. Shim and K. Y. Kim, Design optimization of the impeller and volute of a centrifugal pump to improve the hydraulic performance and flow stability, *ASME Journal of Fluids Engineering*, 142 (10) (2020) 101211.

[18] W. Wang, M. K. Osman, J. Pei, S. Yuan, J. Cao and F. K. Osman, Efficiency-house optimization to widen the operation range of the double-suction centrifugal pump, *Complexity*, 2020 (3) (2020) 1-18.

[19] W. Wang, M. K. Osman, J. Pei, X. Gan and T. Yin, Artificial neural networks approach for a multi-objective cavitation optimization design in a double-suction centrifugal pump, *Processes*, 7 (5) (2019) 246.

[20] J. H. Kim, B. Ovgor, K. H. Cha, J. H. Kim, S. Lee and K. Y. Kim, Optimization of the aerodynamic and aeroacoustic performance of an axial-flow fan, *AIAA Journal*, 52 (9) (2014) 2032-2044.

[21] J. H. Kim, R. Kasahara, T. Kanemoto, T. Miyaji, Y. S. Choi, J. H. Kim, K. Y. Lee and A. M. Galal, Multi-objective optimization of a counterrotating type pump-turbine unit operated at turbine mode, *Advances in Mechanical Engineering*, 2014 (6) (2014) 1-11.

[22] J. H. Kim, J. W. Kim and K. Y. Kim, Axial-flow ventilation fan design through multi-objective optimization to enhance aerodynamic performance, *Journal of Fluids Engineering*, 133 (10) (2011) 101101.

[23] J. H. Kim, D. W. Kim and K. Y. Kim, Aerodynamic optimization of a transonic axial compressor with a casing groove combined with tip injection, *Journal of Power and Energy*, 227 (8) (2013) 869-884.

[24] J. H. Kim, J. H. Choi, A. Husain and K. Y. Kim, Multi-objective optimization of a centrifugal compressor impeller through evolutionary algorithms, *Journal of Power and Energy*, 224 (5) (2010) 711-721.

[25] M. W. Heo, J. H. Kim, T. W. Seo and K. W. Kim, Aerodynamic and aeroacoustic optimization for design of a forward-curved blades centrifugal fan, *Journal of Power and Energy*, 230 (2) (2016) 154-174.

[26] ANSYS CFX-19.0, *ANSYS CFX-Solver Theory Guide*, ANSYS Inc., Canonsburgre, PA, USA (2018).

[27] I. Celik, U. Ghia, P. J. Roache and C. J. Freitas, Procedure for estimation and reporting of uncertainty due to discretization in CFD applications, *Journal of Fluids Engineering*, 130 (7) (2008) 078001.

[28] D. A. Nguyen, S. B. Ma, S. Kim and J. H. Kim, The influence of inlet guide vane and diffuser vane on internal flow characteristics in an axial flow pump, *Journal of Energy Engineering*, 30 (4) (2021) 94-104.

[29] S. B. Ma, S. Kim and J. H. Kim, Optimization design of a twovane pump for wastewater treatment using machine-learningbased surrogate modeling, *Processes*, 8 (9) (2020) 1170.

[30] S. J. Kim, Y. S. Choi, Y. Cho, J. W. Choi, J. J. Hyun, W. G. Joo and J. H. Kim, Effect of fins on the internal flow characteristics in the draft tube of a Francis turbine model, *Energies*, 13 (11) (2020) 2806.

[31] A. Sonawat, Y. S. Choi, K. M. Kim and J. H. Kim, Parametric study on the sensitivity and influence of axial and radial clearance on the performance of a positive displacement hydraulic turbine, *Energies*, 201 (2020) 117587.

[32] J. H. Kim, B. M. Cho, S. Kim, Y. K. Lee and Y. S. Choi, Steady and unsteady flow characteristics of a multi-stage centrifugal pump under design and off-design conditions, *International Journal of Fluid Machinery and Systems*, 12 (1) (2019) 64-70.

[33] A. Afzal and K. Y. Kim, Optimization of pulsatile flow and geometry of a convergent-divergent micromixer, *Chemical Engineering Journal*, 281 (2015) 134-143.

[34] J. C. Helton and F. J. Davis, Latin hypercube sampling and the propagation of uncertainty in analyses of complex systems, *Reliability Engineering and System Safety*, 81 (1) (2003) 23-69.

[35] MATLAB®, *The Language of Technical Computing*, Release 14, the Math Work Inc. (2004).

[36] W. Roux, N. Stander and R. Haftka, Response surface approximations for structural optimization, 6th *Symposium Multidisciplinary Analysis and Optimization Conference*, 534 (1996) 565-578.

[37] J. P. C. Kleijnen, Kriging metamodeling in simulation: a review, *European Journal of Operational Research*, 192 (3) (2009) 707-716.

[38] S. Chen, C. F. N Cowan and P. M. Grant, Orthogonal least squares learning algorithm for radial basis function networks,

IEEE Transactions on Neural Networks and Learning Systems, 2 (2) (1991) 302-309.

[39] D. E. Goldberg, *Genetic Algorithms in Search, Optimization, and Machine Learning*, 13th Ed., Addition-Wesley Professional (1989).

[40] R. H. Myers and D. C. Montgomery, *Response Surface Methodology: Process and Process and Product Optimization Using Designed Experiments*, 2nd Ed., A Wiley-Interscience Publication, USA (2002).

[41] A. Likas, N. Vlassis and J. Verbeek, The global k-means clustering algorithm, *Jounal of the Pattern Recognition Society*, 36 (2) (2003) 451-461.

[42] K. Kan, Y. Zheng, Y. Chen, Z. Xie, G. Yang and C. Yang, Numerical study on the internal flow characteristics of an axial-flow pump under stall conditions, *Journal of Mechanical Science and Technology*, 32 (10) (2018) 4683-4695.

Duc-Anh Nguyen is an integrative student of the University of Science and Technology (UST) and he works at the Korea Institute of Industrial Technology (KITECH) Campus, Korea. He received his Bachelor's degree in aerospace engineering from Ha Noi University of Science and Technology (HUST), Viet Nam, in 2020. His research interests include computational fluid dynamics, turbomachinery, and heat transfer.
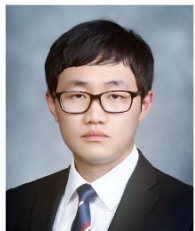
Sang-Bum Ma received his Ph.D. degree from Inha University, Republic of Korea, in 2020. He is currently pursuing his research in fluids engineering at Korea Institute of Industrial Technology (KITECH), Republic of Korea. His researches were mainly for designing turbomachinery by using computational fluid dynamics and design optimization based on machine-learning.

Sung Kim received his Ph.D. degree in Fluid Engineering at Hanyang University, Korea, in 2019. He is currently a Senior Researcher in the Korea Institute of Industrial Technology (KITECH). His research interests are turbomachinery (pumps, fans, compressors, turbines, and pump-turbines) design, numerical analyses, optimization techniques, and experimental tests.

Jin-Hyuk Kim is currently a Principal Researcher at Korea Institute of Industrial Technology (KITECH) and an Associate Professor at University of Science and Technology (UST), Korea. His research interests are fluid machinery (fans, compressors, pumps, hydraulic turbines, and pump-turbines) designs and developments; steady and unsteady numerical analyses; fluid induced vibrations; advanced optimization methods; flow measurements, flow visualizations, and experimental techniques.